The Morphology of Strike-Slip Faults:
Examples from the San Andreas Fault, California

ROGER BILHAM

CIRES and Department of Geological Sciences, University of Colorado, Boulder

GEOFFREY KING

U.S. Geological Survey, Denver, Colorado

Fault zones are seldom straight nor are fractures within them continuous. Permanent strain fields are imprinted near a fault of complex geometry as a result of continued slip. These strain fields may be manifest as vertical deformation near the fault. Strain fields that increase area result in subsidence, and strain fields that reduce area result in uplift. Although these effects are modified by erosion and deposition, the general features of fault zone morphology are a consequence of the geometry and slip distribution along strike. Graphical views of strain fields associated with simple vertical strike-slip faults are derived using boundary element methods. If the fault is straight and parallel to the applied shear strain, the hills and valleys resulting from finite fault rupture are separated by the fault trace. This is rarely observed in nature. Instead, strike-slip faults cut through hills and valleys apparently of their own making. We show this to be a consequence of segments of the fault being nonparallel to each other and to the overall applied shear strain. Coseismic strains are large but transient since they are substantially annulled by rupture on contiguous fault segments. We test our theory with examples from parts of the San Andreas fault system in California. The morphologies of the Parkfield region and the southern San Andreas fault in the Coachella Valley are shown to be consistent with plausible distributions of slip on mapped surface faults. The location of the Salton Sea appears to be a consequence of a reduction of slip on the San Andreas fault toward the Brawley seismic zone.

INTRODUCTION

The spatial distribution of strain surrounding a geological fault was first examined by *Anderson* [1951] more than three decades ago. Since then many workers have reexamined the problem. In particular, *Chinnery* [1961] discussed deformation in a uniform elastic half-space and pointed out that a characteristic distribution of vertical deformation will accompany fault slip. Areal strain contraction results in uplift, and areal strain extension results in subsidence. We model uplift and subsidence around faults in a similar fashion, although we consider that a plate overlying a fluid medium better approximates the mechanical behavior of the upper crust. More recent studies that have influenced our approach and led us to this conclusion include those by *Mansinha and Smylie* [1967], *Savage* [1980], *Pollard and Segall* [1987], *Crouch and Starfield* [1983], *Rundle* [1982], and *King et al.* [1988].

The true constitutive equations governing the behavior of crustal rocks are complex and nonlinear. Indeed, the nonlinearity is such that they probably yield chaotic solutions under most realistic conditions. *Rundle* [1988] has shown that this is true for the time evolution of even a simple example. Nonetheless, provided we attempt only modest predictions using well-defined data, modeling using linear elastic theory is useful. The situation may be compared to forecasting weather. Adequate data and simple models permit adequate short-term forecasting of weather patterns but no realistic data set or complex model can successfully predict such patterns far into the future.

In this article we examine the dilatational strains associated with vertical faults embedded in a horizontal plate and restrict ourselves to posing questions in terms of fault kinematics and simple displacement boundary conditions. We modify the slip on major known or hypothesized features and determine whether the resulting deformation is consistent with secondary features. The method is successful only if we have correctly identified these major features. If field observations have failed to provide such basic information, the modeling is unlikely to predict them correctly. Strictly, the models we present are appropriate for material that is linearly elastic or linearly ductile. Alternatively, they may be regarded as linear approximations to the true non-linear deformation.

We show graphically the form of strain fields that can be associated with individual earthquake rupture and with continued slip on a system of faults. The coseismic strain fields associated with rupture are transient over time scales shorter than the earthquake repeat times whereas the strain fields associated with fault zone geometry are transient over the much longer time scales associated with the persistent bends and offsets. We argue that geometrically induced strain fields, together with the spatial distribution of slip, influence the morphology of the fault zone. A practical use of this relation is that where the long-term distribution of slip on a fault or system of faults cannot be measured directly, it may be possible to estimate the slip distribution from the observed fault zone geometry and morphology.

Examples of the strain fields resulting from idealized fault geometries are presented in order of increasing complexity. We then use combinations of these strain fields to examine the Parkfield region of the San Andreas fault system in central California. Finally, we infer the long term slip distribution on fault segments of the San Andreas system from the morphology of the Coachella Valley region of southern California.

Throughout this paper we are concerned with identifying areas of uplift and subsidence that result from contemporary tectonics. We compare the location of ongoing uplift and subsidence with those developed in our models. Ideally, we might use subsurface contours on some originally horizontal but now deformed surface. In practice, we seek suitable indicators of such contours. Present topography combined with geomorphic indicators of activity are readily interpreted. Thus in the Parkfield region, appropriate contours outlining the shape of the Cholame valley are representative of the area undergoing subsidence. Similarly, present contours indicate the approximate area of uplift near Middle Mountain. In areas other than those we discuss the processes of denudation and sedimentation may occur faster than the tectonic processes we describe. In such regions, surface morphology will be minimal or nonexistent, and it will be necessary to estimate uplift or subsidence rates from the subsurface disposition of stratigraphic horizons of known age and inferred initial shape.

The San Andreas system, like most on-land transform faults, cuts through considerable topographic relief. Throughout its length the location of active fault traces may be identified from morphologic features alone, despite the fact that these features are subdued by surficial processes. In this article we attempt to extend the interpretation of surface morphology beyond that of mapping fault location to obtain an understanding of the distribution of slip and the geometry of the active fault zone at depth.

BOUNDARY ELEMENT MODELS OF STRIKE-SLIP FAULTS

Boundary element methods described by *Crouch and Starfield* [1983] reduce computational demands in the analysis of complex fault geometries by allowing two-dimensional elastic problems to be reduced to one-dimensional problems. We have adopted their computational technique (the TWODD program) but have added features to suit geological problems. Boundary elements may be specified in terms of the relative slip between their surfaces rather than displacement or stress on one side only. We use this in two ways. First, relative slip on an element may be completely specified, and other elements are then required to respond to the resulting stress field. This is a generalized form of a procedure described by *Crouch and Starfield* [1983], that of presetting a uniform strain field or stress field. Second, we may constrain one component of relative slip on an element (the normal component is set to zero in this paper) and allow the other to vary to satisfy a stress condition (in this paper the tangential stress is set to zero).

The boundary elements used by *Crouch and Starfield* [1983] have a constant slip, and consequently, several contiguous elements must be used to simulate nonuniform slip. The program permits the use of elliptical slip distributions derived from expressions of *Pollard and Segall* [1987], although in this paper we use this option only to specify slip on the single fault segment in Figure 2. Computation time is proportional to the number of fault segments and to the desired spatial density of strain and displacement data. The models that follow were each computed on a portable 32-bit computer in a few minutes. The program permits the computation of the dilatational or shear strain fields surrounding any number of fault segments on which strike-slip or normal displacement may be specified. For example, a strike-slip fault may be specified with pure shear or with shear combined with a component of opening or closing to simulate real conditions in fault zones.

The region of interest may be subjected to a uniform strain condition by imposing appropriate displacements outside the area under investigation. For example, it is appropriate in models of parts of the San Andreas fault system to impose a right-lateral shear to the region prior to modeling slip on known faults. Of considerable importance is the ability to introduce a fault within the region of interest and to permit it to slip freely in response to strain fields created by motion on distant boundaries and on adjacent faults or fault segments. The conditions on a free fault are zero tangential stress and zero relative normal displacement between the fault faces. It has been suggested that a fault should respond to distant boundaries and to adjacent faults according to some frictional law. This is incorrect for systems where the distant boundaries are subject to displacement conditions or the motion on adjacent faults is specified in terms of slip. For example, suppose the slip between distant boundaries is V and the cumulative slip on the *free* fault is d. As V increases, d also increases, and the slip deficit, $(V-d)$, never becomes large. For large values of V and d the quantity $(V-d)$ becomes small compared to V. A condition of zero tangential stress on the free fault best approximates this condition rather than a friction law which causes $(V-d)$ to increase in proportion to V. For a further discussion, see *Rundle* [1988].

Definitions and Procedure

In the following account a fault segment is considered to be a continuous fault that is assumed to be straight to within 1% of its length. The strike of a fault segment relative to the displacements applied at a plate boundary will be referred to as the obliquity of the fault segment. A bend in a fault zone is thus the difference in strike of contiguous fault segments. An offset in a fault zone occurs if two adjoining parallel fault segments are not colinear.

In the plan view models that follow we first apply a shear strain to the area shown. This shear strain is created by imposing an antisymmetric displacement condition parallel to the upper and lower boundaries of the model at a large distance from the fault. To emulate "realistic" plate boundary conditions, the sum of the displacements on these two "distant" boundary elements is equal to or less than the maximum slip later introduced on fault segments. That is, the fault displacement never exceeds the plate boundary displacement. Fault segments are introduced into the model as straight-line boundary elements by specifying their starting and ending x,y coordinates and assigning a value for fault-parallel slip and sometimes a value for fault-normal slip. More complex slip distributions are introduced by specifying contiguous boundary elements with different displacements. For each point of the area shown we calculate a value for dilatational strain by summing strains resulting from each boundary element. These include the two distant boundary elements and all fault segments under investigation. The strains in the region are assigned an appropriate grey scale weight for plotting. Dark areas correspond to areal strain extension and light areas correspond to areal strain contraction. An intermediate grey background signifies little or no areal strain. The strain data are output to a computer screen from which a printed replica is made. These "screen dumps" have been annotated in the figures to illustrate the kinematics of the models.

Since we are viewing a free surface in a uniform material, the effect of nonzero Poissons' ratio is to cause the extensional areas to become valleys and the areas of contraction to become hills. Uplift and subsidence can be quantified if we make assumptions about the effective elastic thickness of the crust, the distribution of density with depth, and erosion and deposition rates. For example, if the elastic crust consists of a plate of thickness h and calculations are in generalized plane stress, then changes of thickness Δh are related to horizontal strains by

$$\frac{\Delta h}{h} = \varepsilon_{zz} = \left(\frac{-\nu}{1-\nu}\right)\left(\varepsilon_{xx} + \varepsilon_{yy}\right)$$

$$\Delta h = h\left(\frac{-\nu}{1-\nu}\right)\left(\varepsilon_{xx} + \varepsilon_{yy}\right)$$

where ν is Poissons' ratio, the z axis is vertical, the x and y axes are horizontal and the corresponding linear strains are ε_{zz}, ε_{xx} and ε_{yy}. Volume is conserved if Poissons' ratio is 0.5. The proportion of plate thickening or thinning that appears as uplift or subsidence depends on the degree of isostatic compensation. In the caption to Figure 1 we indicate numerical values for uplift and subsidence, given reasonable values of the foregoing parameters. Similar values apply to later figures. Maximum uplift values of between 10 and 100% of the associated fault slip are reasonable. Although adequate data will allow more precise numerical estimates for uplift, these considerations are secondary to the thrust of this article. We are concerned more with the general form and location of strain fields surrounding a strike-slip fault than in the absolute magnitudes.

Fig. 2. Strike-slip fault with an elliptical distribution of slip. See Figure 1 for key to shading.

Strain Fields Associated With Simple Strike-Slip Structures

Figure 1 shows the strain field resulting from slip that is uniform along strike. The figure is a plan view of the fault where dark areas correspond to areal strain expansion and the light areas correspond to areal strain contraction. Light areas correspond to uplift and dark areas to subsidence. The strain field in Figure 1 is antisymmetric about the fault. That is, the fault separates hills from valleys.

Slip on a fault is rarely uniform along its length. The fault shown in Figure 2 has an elliptical distribution of slip with a maximum at the center and a minimum at each end. The strain field is now distributed along the fault zone rather than concentrated near the ends.

A less symmetric slip distribution produces the strain field of the form shown in Figure 3. In this case, five contiguous segments are
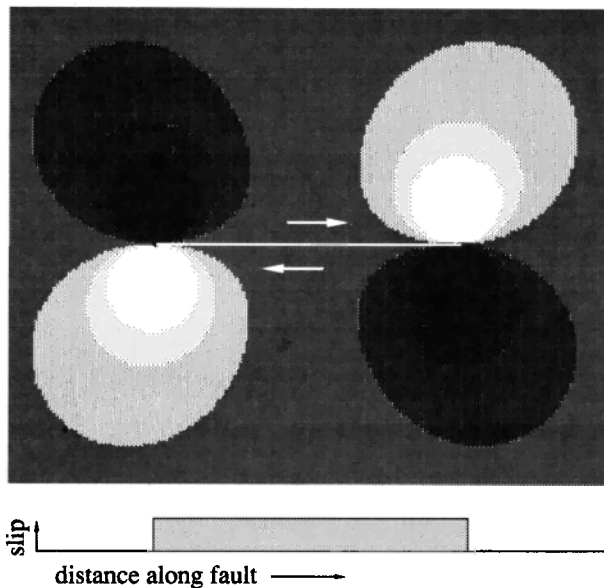

Fig. 1. Areal dilatation due to uniform slip on a vertical strike-slip fault in a plate of uniform thickness. In this and all subsequent plots, two shades of dark grey and black are used to indicate areal extension, and two shades of light grey and white indicate areal contraction. Dark shading corresponds to strains ($\varepsilon_{xx} + \varepsilon_{yy}$) greater than 2.5, 5.0, and 7.5%, respectively, for a fault with a displacement of 10% of its length; for example, 1 km in 10 km. Light shading represents equivalent strain increments for negative values. For a plate thickness of 10 km and a Poissons' ratio of 0.5, black areas correspond to thinning that exceeds 750 m and white areas correspond to thickening of more than 750 m. Within these regions, for a 10-km-long fault, the thickening and thinning can exceed the fault slip. The background grey corresponds to regions where the plate thickness does not change by more than 250 m. As the text explains, uplift and subsidence in the real Earth cannot be determined directly from plate thickening without some allowance for other parameters. Nonetheless, it is reasonable to suggest that maximum uplift and subsidence is approximately equal to the associated fault slip. Plausible alternative values of Poissons' ratio, plate thickness, and the effects of isostatic compensation might in some cases reduce this to 10% of fault slip.
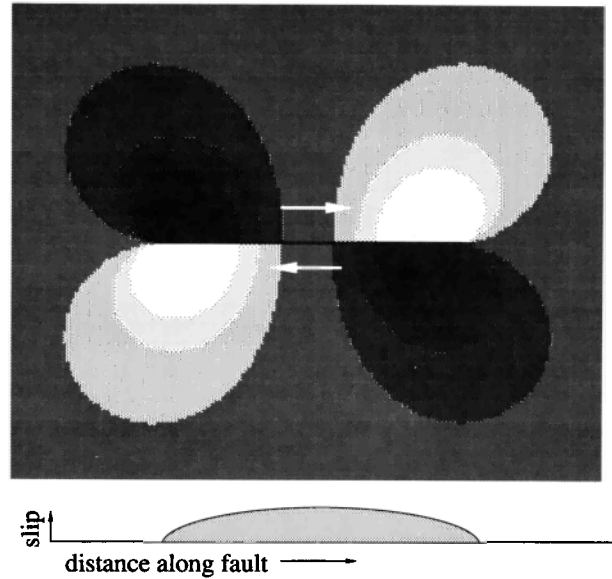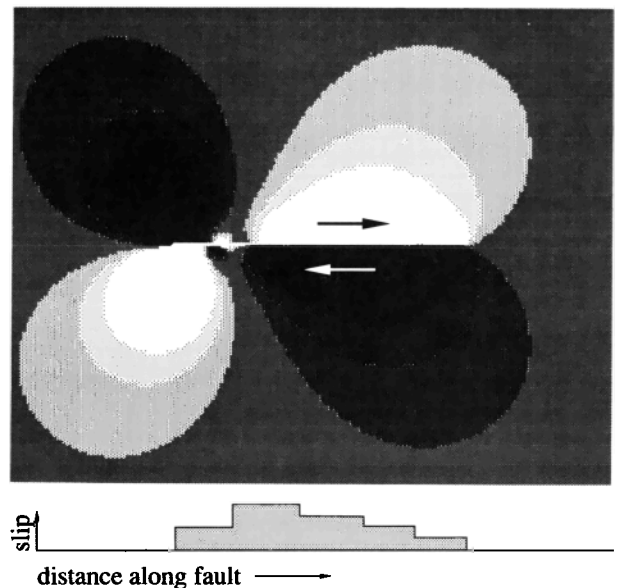

Fig. 3. Strike-slip fault with asymmetrical non uniform slip. See Figure 1 for key to shading.
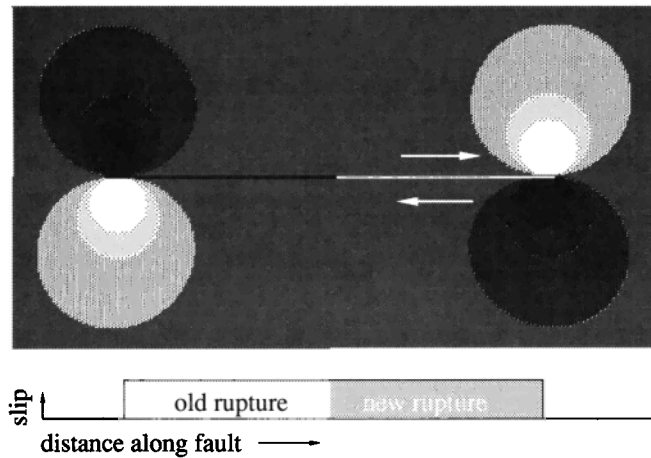
Fig. 4. Contiguous uniform rupture of straight fault in two earthquakes. See Figure 1 for key to shading.

made to slip different amounts along strike, with maximum slip occurring to the left center of the rupture. The distribution of strain reflects this nonuniform slip.

A recurring nonuniform distribution of coseismic slip on a fault is one of the criteria for recognizing "characteristic" earthquakes [*Schwartz and Coppersmith*, 1984]. If the surface distribution of slip persists at depth, then strain fields of the type shown in the figure will grow with time. However, the strain field arising from a characteristic earth-quake cannot be considered in isolation. The long-term strain field includes contributions from contiguous or adjacent fault segments.

We now consider the affects of motion on contiguous sections of a single straight fault. Earthquakes on contiguous parts of a fault will cancel the termination strain fields associated with individual earthquakes if slip at their point of contact is the same. Imagine two identical strain fields, as shown in Figure 1, caused by rupture of adjacent fault segments each with equal uniform slip. Provided the fault is straight and the slip is uniform, there will be zero net strain at their point of contact. The resulting strain field will appear as shown in Figure 4.
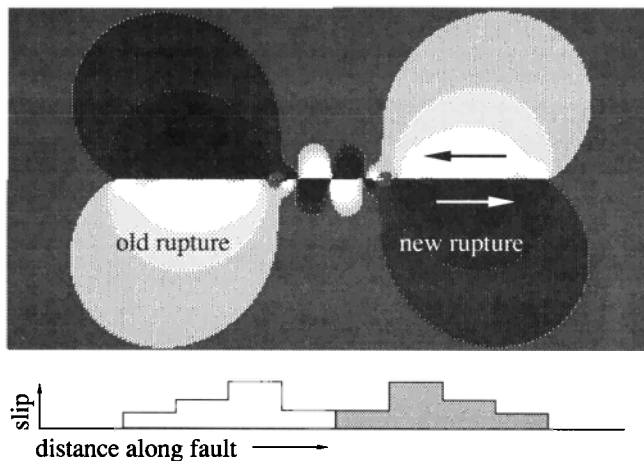

Fig. 5. Contiguous heterogeneous rupture of a straight fault. Two contiguous ruptures have slip distributions similar to those shown in Figure 3. Note that the strain field is not cancelled where the two ruptures meet as it is in the uniform slip case of Figure 4. Deformation will progressively increase in amplitude and retain the same form if repeated rupture occurs. See Figure 1 for key to shading.
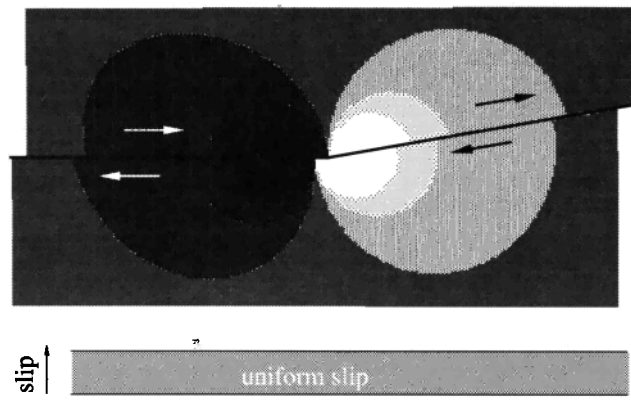

Fig. 6. Dilatational strain at a bend between two fault segments. See Figure 1 for key to shading.

Rupture of contiguous fault segments in events with persistent irregular slip distributions, however, will imprint a strain field related to the combined slip deficiencies along the fault (Figure 5). The net strain field contains no information concerning the termination of rupture of individual events since it could represent the slip of one event with a slip distribution equal to the sum of the individual events. In this example, however, if the behavior of one segment is known, features of the second may be inferred.

The models we have presented so far consider only the permanent deformation that must occur as a consequence of changing slip amplitude on a straight fault. Changes in the orientation of slip vectors due to changes in fault strike also produce permanent deformation [*King*, 1986; *Bilham and Hurst*, 1988]. Figure 6 shows the effect of a bend between two long fault segments that differ in strike by 9°. Identical right-lateral slip occurs on each of the two fault segments. Note that the regions of uplift and subsidence now lie on the faults.

A field observation relevant to bends in fault zones is that fault slip is reduced on segments that are not parallel to the slip vector [*Bilham and King*, 1989]. The strain field in Figure 7 illustrates the effect of reducing slip by a factor of 2 at a 9° bend in a fault zone. This geometry and slip distribution is appropriate to the 1906 San Francisco earthquake near Black Mountain [*Thatcher and Lisowski*, 1987]. Regions of uplift and subsidence still cross the faults but are no longer centered on them. Areas of strain contraction are predicted
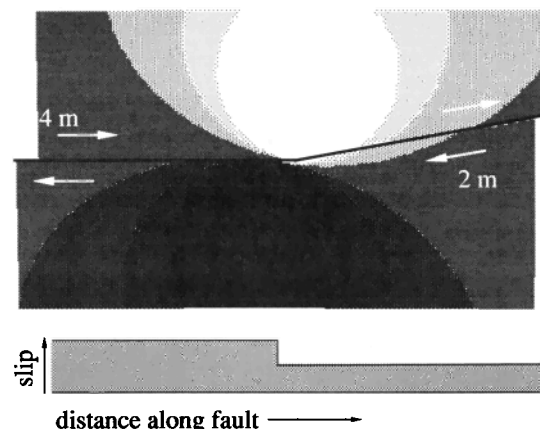

Fig. 7. Strain associated with reduced slip at a bend. See Figure 1 for key to shading.

within the reentrant angle of the bend. As the reduction of slip increases, the strain distribution tends toward that shown at each end of the rupture in Figure 1.

The strain field due to a locked section between two slipping fault segments is shown in Figure 8. This strain field is the extreme case of a slip deficit along strike.

An offset in the fault zone (Figure 9) results in a strain field similar to that shown in Figure 8, but the zones of areal strain contraction (light shading) merge across the fault. If the offset were a releasing offset (i.e., the same geometry but a left-lateral fault) the contraction and extension would be reversed, resulting in subsidence crossing the fault zone. The structures produced correspond to compression ridges and sag ponds.

The strain fields associated with oblique segments within a fault zone are shown in Figure 10. The size of the strain field is proportional to the length of the oblique segments defining the offset. Note that, provided slip is equal in the two nonoblique segments, the faults cut through the hills or valleys they create. This is to be compared to the models of straight faults with zero obliquity where the fault separates the hills and valleys associated with nonuniform slip. The effect of increasing segment obliquity under conditions of identical slip on each segment is illustrated in Figure 10.

The foregoing assumes that all off fault deformation obeys the rules of linear elasticity. If the region close to and including the fault deforms more readily than other regions, no strain field will be

Fig. 9. Strain field at an offset in a fault zone. The slip on each trace is identical. See Figure 1 for key to shading.

generated by slip along the fault except within that zone. To demonstrate this effect we introduced an oblique fault segment on which we specified strike-slip and fault-normal displacement (Figure 11). Suppose the model in Figure 11 represents two blocks that are free to slide in a left-lateral sense. The oblique fault in this case represents an "air gap" which widens normal to the fault by $s \sin \phi$ for each increment in slip s along the adjoining slip-parallel segments. The boundary element model in Figure 11 represents the effect of slip s in the opposite (right-lateral) sense, causing fault-normal conver-
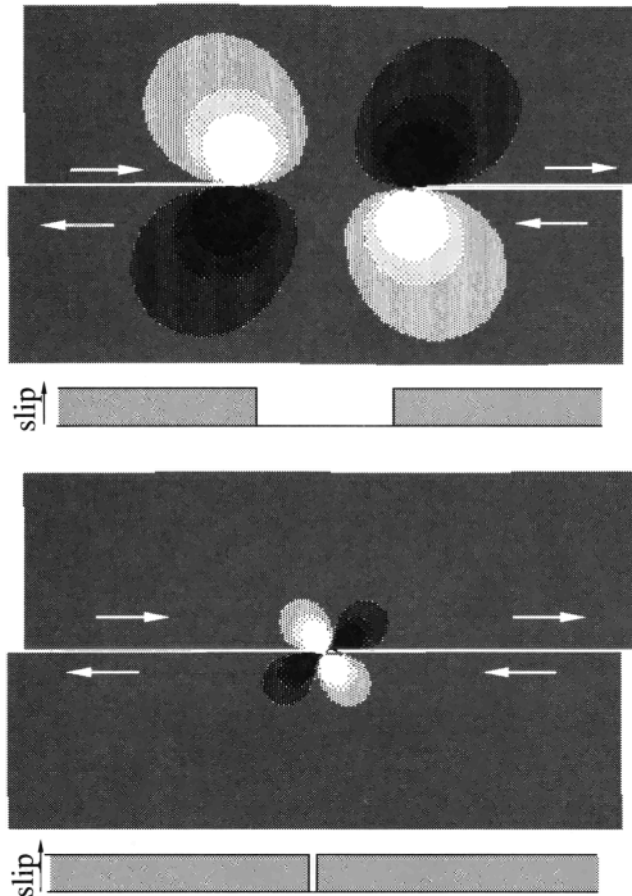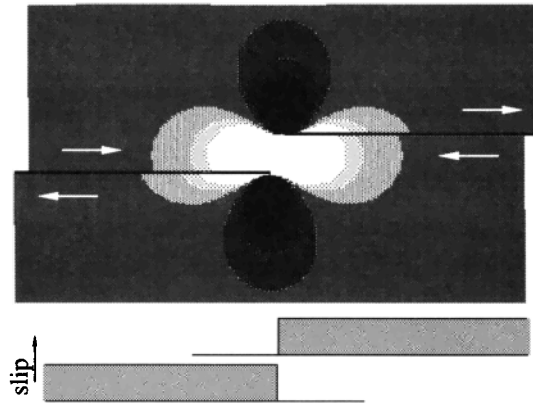

Fig. 8. Strain fields associated with locked patches between two segments of a right-lateral fault that slips similar amounts. The slip is the same in each example, but the intervening locked patch is much shorter in the lower figure. The strain fields cancel as the locked patch length tends to zero. See Figure 1 for key to shading.
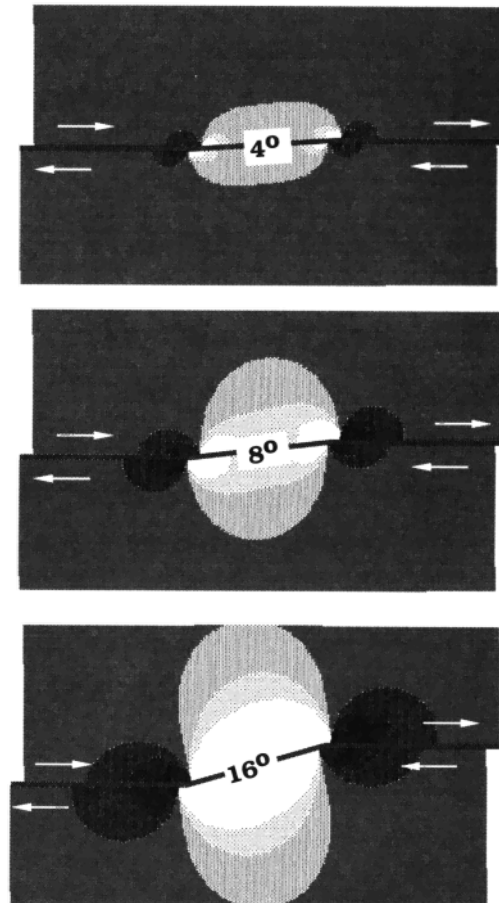

Fig. 10. Change of dilatational strain resulting from increased segment obliquity. Slip amplitude is identical in each example and uniform along the strike of all the fault segments. See Figure 1 for key to shading.
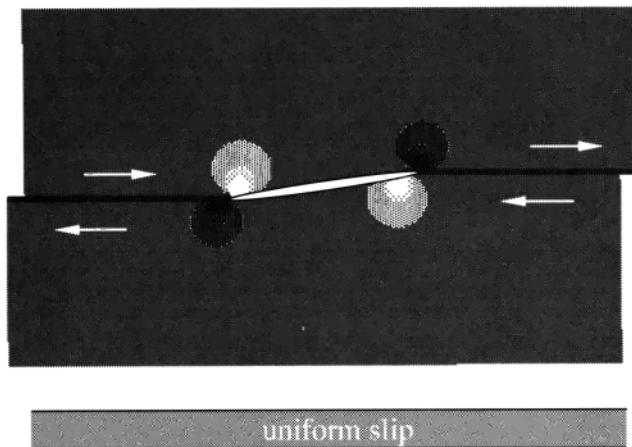
Fig. 11. An oblique fault segment with areal strain contraction entirely accommodated within a narrow zone. The residual strains are associated with bends in the fault. See Figure 1 for key to shading.

gence ($s \sin \phi$) on the oblique segment. The large dilatational strains evident in Figure 10 are now concentrated within a narrow area which we represent as an ellipse along the fault in Figure 11.

Under reasonable assumptions, Figures 10 and 11 may be regarded as extreme cases. If we assume that deformation in the Earth results in effective "work softening" and not "work hardening", then Figure 10 represents the widest zone of likely deformation and Figure 11 represents the narrowest reasonable strain field centered on a fault. As we indicate schematically in Figure 11, displacement normal to the fault cannot realistically be accommodated by a fault zone of zero width. In practice, the deformation in such regions appears to be accommodated by dip-slip features and flower structures [Sylvester and Smith, 1976, Bally, 1983]. Such features were apparently active during the aftershock sequence of the 1984 Morgan Hill, California, earthquake [Oppenheimer et al., 1988].

Combinations of fault slip and offset may now be considered. Each view in Figure 12 represents an identical geometry for a strike-slip fault subject to different amounts of slip (indicated numerically). Slip is uniform along the fault in the upper figure. In the central and lower views in Figure 12, fault slip decays incrementally from left to right. The central view of the strain field shows a lower reduction of slip from left to right than the bottom view. Note that the strain field is symmetric for uniform slip only (e.g., Figure 10). As slip decays along strike, the extensional and contractional strain fields become increasingly antisymmetric and begin to resemble the rupture termination strains evident in Figures 1-3.

In Figure 12 the decay in slip is monotonic. If slip on oblique segments is less than that on adjoining slip-parallel segments (refer also to Figure 7), the predicted strain fields surrounding the segment are complicated further. Figure 13 shows the asymmetry induced by one such distribution of slip.

Summary of Theoretical Uplift Results

We summarize the results as follows. Uniform slip along a straight fault results in a strain field in which the fault divides zones of vertical deformation that are of opposite sign. Nonuniform slip adds detail to the strain field but leaves the symmetry unchanged. If the surface slip distributions of "characteristic" earthquakes persist to depth they will influence fault zone morphology, but this can only be interpreted if the behavior of adjacent faults is known. The strain
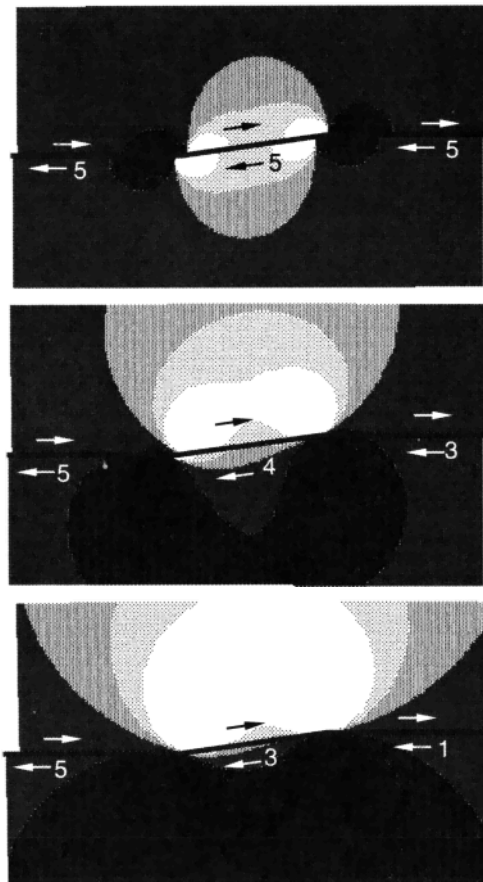

Fig. 12. Effect of varying slip along strike near an oblique fault segment. In the upper figure slip is uniform. In the lower two figures slip is reduced along strike as indicated by numeric values. See Figure 1 for key to shading.

fields that produce this morphology in the long term differ from coseismic strain fields, because they are the sum of the strains of contiguous fault segments that move at different times. The long-term strain field is further modified by bends between fault segments.
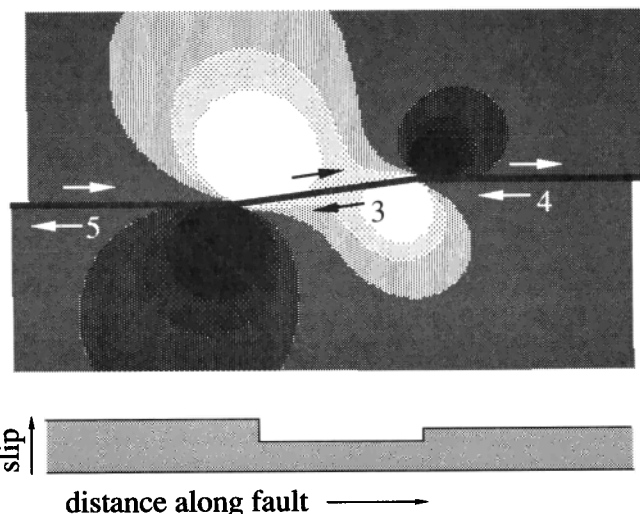

distance along fault ⟶

Fig. 13. The strain field associated with reduced slip on an oblique segment. Relative slip along strike is indicated numerically and graphically. See Figure 1 for key to shading.
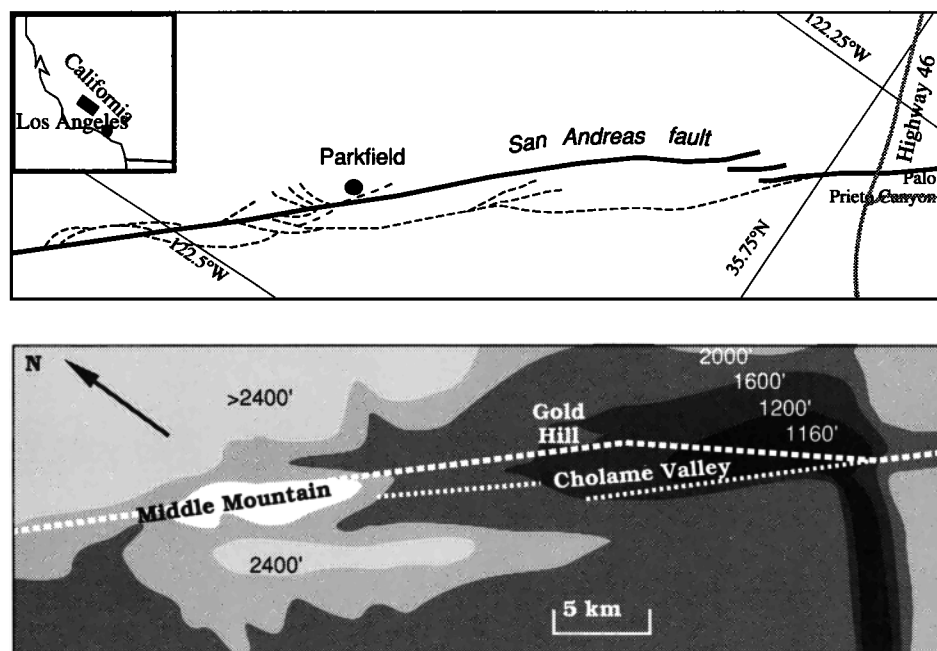
Fig. 14. Location map and principal mapped faults in the Parkfield region. Thick dashed lines in the lower topographic sketch show the main trace of the San Andreas Fault used in subsequent models. Thinner dashed lines shown the location of the simplified set of subsidiary faults used in the models. Contours in feet; the base of the Cholame Valley is at 1160 feet (354 m) and the summit of Middle Mountain exceeds 2800 feet (933 m).

In particular, long-term strain fields along geometrically complex faults are not symmetrically disposed about the fault zone. Faults cut through the hills or valleys that they create. The rate of growth of fault zone features in the models can be estimated (see the example in the Figure 1 caption), although the inclusion of the effects of erosion and sedimentation requires detailed data and modeling that are outside the scope of this paper. In this study we are concerned principally with the location and general form of fault zone features, and we ignore the modification of these features by surficial processes.

APPLICATION OF BOUNDARY ELEMENT MODELS TO THE SAN ANDREAS FAULT ZONE

We now apply our understanding of the "building blocks" of fault zone morphology, discussed in the previous section, to parts of the San Andreas fault zone in California.

Parkfield, Central California

The Parkfield region has been the subject of special study by the U.S. Geological Survey because of the recurrence of M≈6 earthquakes at intervals of a few decades [Bakun and Lindh, 1985]. The region embraces a 30-km length of the San Andreas fault between the creeping section of the San Andreas fault to the northwest [Schulz et al., 1982] and a section to the southeast that has not moved since 1857 but has moved repeatedly in large earthquakes [Sieh, 1984].

The topography of the Parkfield region, simplified from 7.5' quadrangle maps, is shown in Figure 14. In the map we use the same sign convention as that applied to the boundary element models: high ground is shown as white and low ground is mapped as black. Figure 14 shows some of the numerous mapped faults in the region [Brown et al., 1967] and the simplified fault trace that we use to examine dilatational strain resulting from fault activity. The fault shown

along the southwest side of the Cholame valley is taken from Dickenson [1966] and Dibblee [1973]. The fault trace is most notably simplified at the southeast termination of the fault zone where, at the time of the last earthquake, several en echelon surface fractures appeared in the Cholame valley. We use the fault geometry shown in Figure 14 as input to the boundary element models in Figure 15.

In Figure 15 we present three models. The coseismic strain field anticipated from a single Parkfield earthquake, or a sequence of identical earthquakes, is shown in Figure 15a. It has characteristics similar to Figure 1, with termination strains at Middle mountain and the southern end of the Cholame valley. The computed uplift and subsidence does not match the topography. In Figures 15b and 15c the entire San Andreas fault is permitted to slip uniformly from north of the region to south of the region but with a 20% deficit where the fault crosses the Cholame valley. Details of the modeled fault traces are listed in Table 1. In Figure 15b the main fault only is modeled. In Figure 15c, subsidiary mapped faults on the southwest side of the Cholame Valley are permitted to slip freely. If these two figures are compared to Figure 14, it will be noted that there is a close resemblance to the topography near to the fault. The fit is better for Figure 15c than Figure 15b. The Cholame Valley appears to be the result of a dilatational "hole" caused by the overall offset in the fault zone at this point. Middle Mountain is centered on a dilatational hill. The models fail to generate high ground further to the northeast and southwest of the fault. These features are geologically older than features within 5 km of the fault zone [Dickenson, 1966], and we do not consider that they result from the current fault geometry and slip.

In addition to emulating the principal morphologic features of Figure 14 the models shown in 15b and 15c are consistent with two minor observations in the region. The first of these is that the models suggest that Gold Hill is the result of ongoing uplift. Second, uplifted river terraces (see Figure 14) are to be found in the Palo Prieto Canyon near the southern end of the Cholame valley. These are
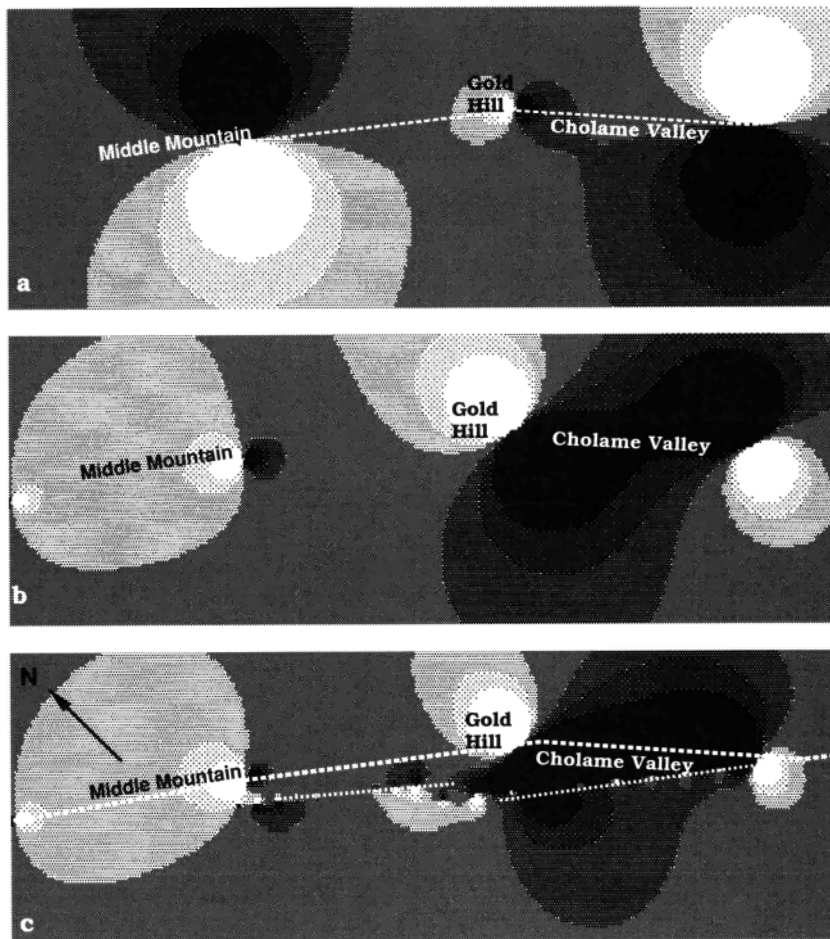
Fig. 15. Models for slip in the Parkfield region. (a) shows the strain field anticipated from 1966-type rupture at Parkfield on indicated faults. The fault is assumed locked to the NW and SE. Note that this deformation field does not emulate the topography shown in Figure 14. Figures (b) and (c) show the strain fields resulting from throughgoing slip to the NW and SE, and slip on indicated faults (dashed lines). Details of the boundary elements used in the models are found in Table 1. The strain field in Figure 15c is a reasonable fit to the topography in Figure 14. See Figure 1 for key to shading.

TABLE 1. Boundary Element Model Parameters for Figure 15.

	x Start	y Start	x End	y End	Strike slip	Element
1	50	500	50	-500	-0.0175	NE slip boundary
2	-50	-500	-50	500	-0.0175	SW slip boundary
3	1	2.1	1.45	6.1	0.025	
4	1.45	6.1	1.2	9.55	0.020	
5	-0.6	-20	-0.6	-8	0.025	
6	-0.6	-8	0.4	-1.3	0.025	
7	0.4	-1.3	1	2.1	0.025	
8	1.2	9.55	1.3	11.4	0.020	
9	1.3	11.4	2	18	0.025	
10	0.7	5	1.2	9.55		segment free to slip, nine elements
11	0.6	2	0.9	4.6		segment free to slip, nine elements

The x and y coordinates indicate the start and end points of boundary elements. The amount of strike-slip is indicated numerically. Positive strike slip is right-lateral motion. The first two elements indicate the remote boundary elements that impose right-lateral shear on the study region; elements 3 to 9 represent the main trace of the San Andreas fault. The geographic origin of the coordinate system (0, 0) is 120°32.5' West and 35°57.5' North. Scale and azimuth is indicated by coordinate (0, 12), which corresponds to 120°15' West and 35°37.5' North. Figure 15a used elements 1 to 4. Figure 15b used elements 1 to 9. Figure 15c used elements 1 to 11.

consistent with the geometrically induced strain field imprint but not with the coseismic strain field which demands subsidence in this region.

The Southern San Andreas Fault

In Figure 16 we show the topographic and tectonic setting of the Salton Trough [*Sharp*, 1983]. The southern San Andreas fault in the Coachella Valley in southern California has not experienced a major earthquake in historic time, although its potential for slip is considered high [*Sykes and Nishenko*, 1984; *Stuart*, 1986]. Present seismicity is insignificant, but the fault trace is mapped in great detail [*Clarke*, 1984] and is sufficiently well defined to host a number of creepmeters that indicate creep of a few millimeters per year [*Louie et al.*, 1975]. The fault underwent accelerated creep (triggered slip) in 1968, 1979, and 1986, shortly after the occurrence of large local earthquakes [*Williams et al.*, 1989]. Triggered slip was shown to be restricted to oblique fault segments [*Bilham and Williams*, 1985] in the Coachella Valley cutting topographic highs of recent uplift: Mecca Hills, Indio Hills, and Durmid Hill. The southernmost mapped portion of the San Andreas fault disappears near Bombay Beach on the shores of the Salton Sea where it meets the Brawley seismic zone; a diffuse region of sporadic microearthquake swarm
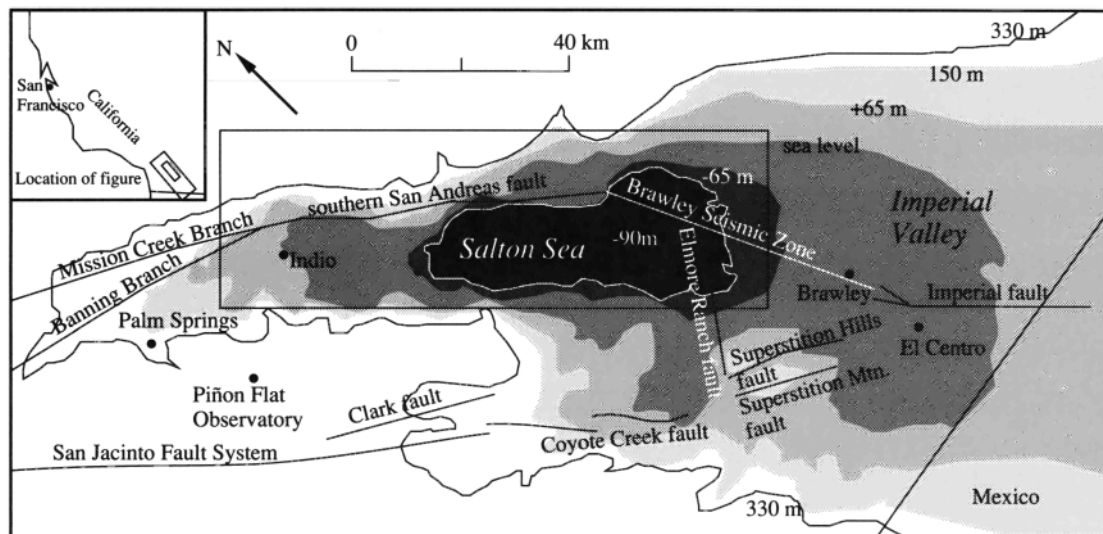
Fig. 16. Simplified fault map and topographic features of the Coachella and Imperial Valleys of southern California. Above the 330 m contour the ground rises sharply in the form of ancient basement rocks. Much of the basin contains thick Quaternary sediments.

activity that extends southward to the Brawley fault and the Imperial fault [*Johnson and Hill*, 1982].

The Brawley seismic zone is 50 km long, not more than 10 km wide, and has been described as the most northerly of a series of spreading centers that continue to the south in the Gulf of California [*Lomnitz et al.*, 1970]. The region is the locus of high heat flow and recent volcanism described in detail by *Lachenbruch et al.* [1985]. *Fuis et al.* [1984] show that the 5-km-thick sediments in the Salton Trough are underlain by a 7-km-thick low velocity basement interpreted to consist of metasediments. There appears to be no local seismic velocity anomaly associated with the Brawley seismic zone.

The rectangular region outlined in Figure 16, which is the focus of our models (enlarged in Figure 17), includes three hills cut by the San Andreas fault (Indio, Mecca, and Durmid). Each of these hills is considered to be locations of active tectonic transpression [*Sylvester*, 1988] as a consequence of oblique slip. The base of the Salton Sea is approximately 90 m below mean sea level. The location of the Salton Sea to the southwest of the fault and high ground to the northeast of the San Andreas fault is suggestive of a rupture termination strain field with uplift on one side of the fault and subsidence on the other. The fault does not exactly divide uplift from subsidence, however, and the uplifted region is more localized than the region of subsidence.

In the following models we use the geometric shape of the segmented southern San Andreas fault zone (Figure 17) as described by *Bilham and Williams* [1985]. Figures 18 and 19 show some plausible fault slip distributions, with corresponding numeric parameters listed in Table 2. In Figure 18a, uniform slip is allowed to extend down the San Andreas and into the Brawley seismic zone. In Figure 18b, slip terminates at the southern end of the San Andreas and none is accommodated in the Brawley seismic zone. In Figure 18c, slip on the San Andreas is equally partitioned between the Brawley seismic zone and an inferred southern extension to the San Andreas fault.

All of these models contain elements of the topography shown in Figure 16b, but none adequately explains the observed features. The model shown in Figure 18a shows compressional hills developing at the Indio segment, the Mecca segment, and the Durmid Hill segment but indicates no subsidence in the region of the Salton Sea. Figure 18b produces a circular basin at the lowest point of the Salton Trough but does not produce low ground to the southeast of the intersection of the southern San Andreas and Brawley seismic zone. Figure 18 shows hills in their correct locations on the fault zone and low elevations to the southwest of Durmid Hill but shows no topographic low in the region of the Salton sea.

In Figure 19, in addition to invoking reduced slip on the Brawley
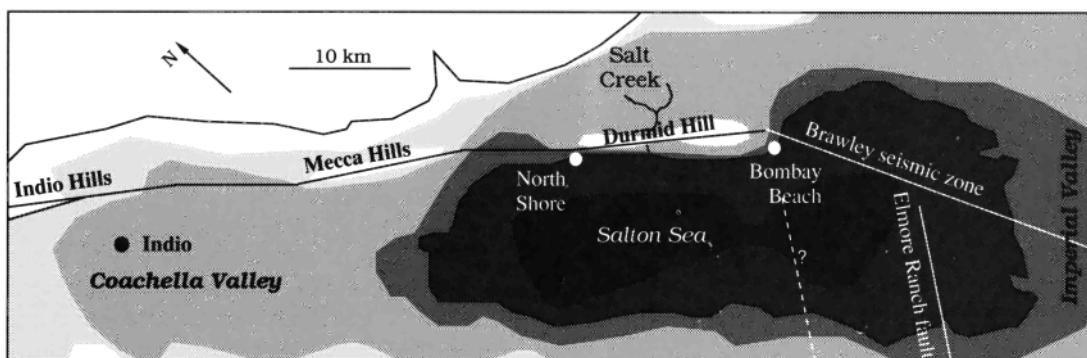

Fig. 17. The principal geomorphic features of the southern San Andreas fault and associated faults in the Coachella Valley. An inferred fault is indicated parallel to the Elmore Ranch fault close to Bombay Beach.
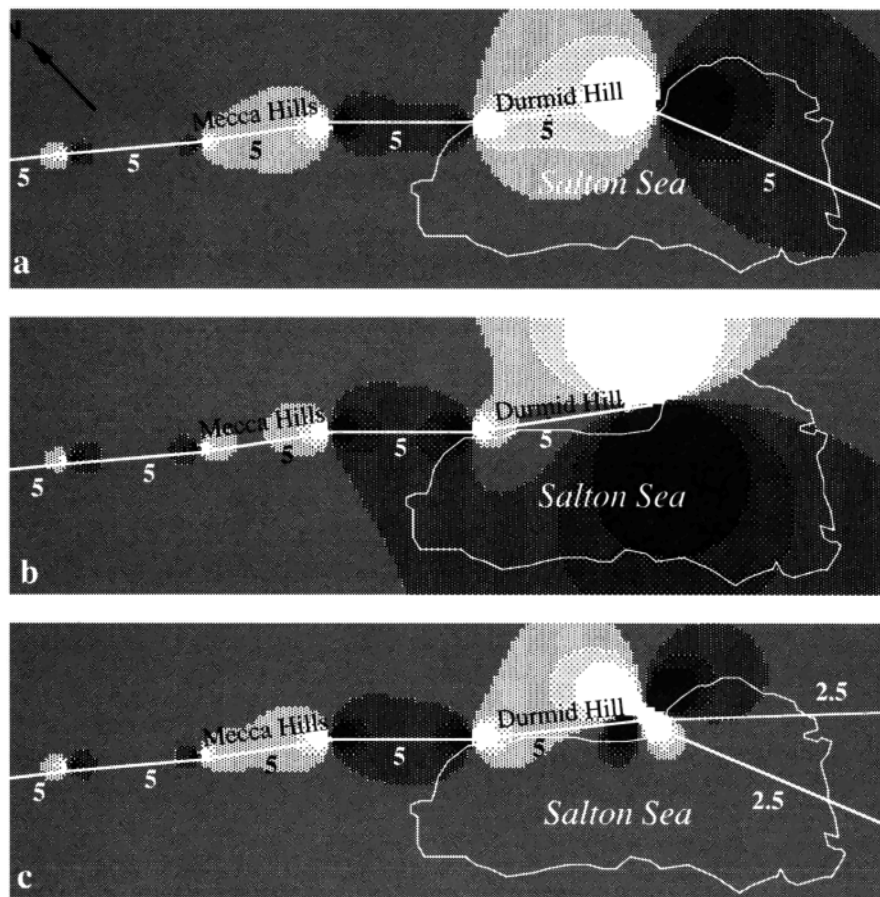
Fig. 18. Dilatational strain fields resulting from different distributions of slip on segments of the southern San Andreas fault and Brawley seismic zone. (a) Uniform slip on the San Andreas fault and the Brawley seismic zone. (b) Slip terminated on the southern San Andreas fault with no slip on the Brawley seismic zone. (c) Slip equally distributed between the Brawley seismic zone and an inferred SE extension to the southern San Andreas fault. Compare Figure 18 with the topography shown in Figure 17. Numerical values indicate relative displacement in each segment (see Table 2). See Figure 1 for key to shading.

seismic zone, we attempt to simulate the observed topography by reducing slip southward on the southern San Andreas fault. We are guided in doing this by the resemblance of the topography to a rupture-termination type of strain field, referred to earlier. In Figure 19a we reduce slip uniformly by a factor of 2.5 between the Indio Hills and Durmid Hill. This does not produce the Salton trough. In Figure 19b the Salton trough appears when slip is reduced in the limited region between North Shore and Bombay beach. In Figure 19c we introduce two cross faults (the Elmore Ranch fault and an additional subparallel fault) that are permitted to slip freely in response to motion on the southern San Andreas and the Brawley seismic zone. Figures 19b and 19c both reproduce the main features of the topography, although Durmid hill is modeled to be wider than the observed feature. We note that the Bishop Tuff mapped on the surface of Durmid Hill is found at a depth of 1704 m in the State 2-14 Borehole, near the center of the Brawley seismic zone [Herzig et al., 1988]. The age and depth of this stratigraphic horizon suggests a subsidence rate in the Salton Trough of 2.4 mm/yr, similar in magnitude to the 3±1 mm/yr uplift rate estimated for Durmid Hill [Bilham and Williams, 1985].

DISCUSSION

Our models of the San Andreas fault in central and southern California suggest that changes of strike of the fault help determine fault zone morphology. The locations of Middle Mountain in the Parkfield region and the Indio Hills, Mecca Hills, and Durmid Hill in the Coachella Valley are correctly predicted with faults cutting through them. The areas of strain contraction in the models are larger spatially than is evident from the regions of uplift observed in the field. This may result from materials near the fault zone being more readily deformed than surrounding materials or to Middle Mountain and Durmid Hill containing blind reverse faults that we have not modeled. On the other hand, the spatial extent of zones of subsidence is much better emulated by our models. Thus the aspect ratios of the Cholame Valley and the Salton Sea are similar to the corresponding zones of subsidence evident in our models.

Although earthquakes are known to repeat along the Parkfield segment of the San Andreas fault, there is little or no evidence for this in the topography. The 20% reduction of long-term slip in the Cholame valley could be associated with the offset repeatedly acting to terminate rupture for individual earthquakes, but our modeling is not sufficiently unique to be certain that the reduction in slip is real. We could be ignoring significant effects due to erosion or deposition of sediment. Moreover, we may have ignored active faults that are presently unmapped or assumed to be inactive.

The most significant finding in our models of the southern San Andreas is that they suggest that substantial slip on the Brawley seismic zone is inconsistent with the formation of the Salton Sea basin. Models (not shown) in which we permitted the Brawley seismic zone to act as a perfect "spreading center," keeping pace with
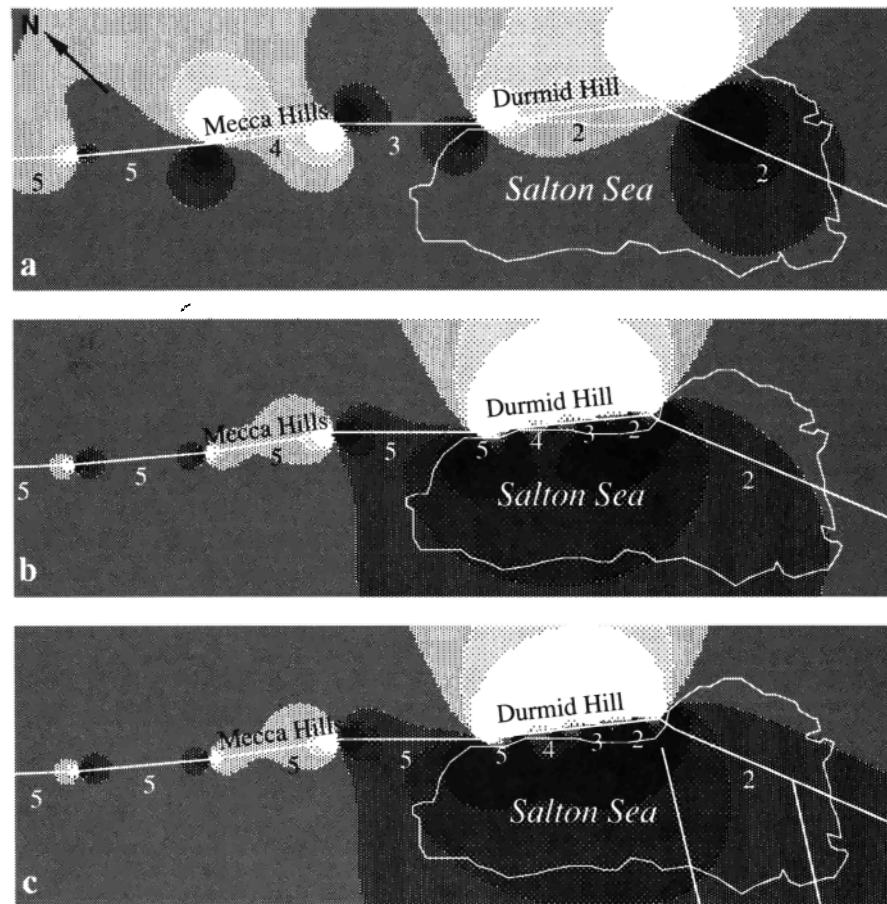
Fig. 19. In each of the three figures, slip is reduced by a factor of 2.5 between the Indio Hills and the Brawley seismic zone. (*a*) Slip decay is uniform and linear. (*b*) and (*c*) Decay occurs entirely within the Durmid Hill segment. In Figure 19*c* two cross faults have been permitted to slip freely (which they do in a left-lateral sense). Compare Figure 19 with the topography shown in Figure 17. See Figure 1 for key to shading.

TABLE 2. Boundary Element Parameters for Figures 18 and 19.

	x Start	y Start	x End	y End	Strike Slip	Normal Slip	Element
1	250	-60	-150	-60	-0.025	0.002	slip boundary
2	-150	30	250	30	-0.025	0.002	slip boundary
3	104	-26.9	160	-8	0.05	0	Brawley seismic zone
4	-30	-10.5	50	-21.7	0.05	0	Banning Fault
5	50	-21.7	62	-22.7	0.05	0	Coachella Canal
6	62	-21.7	74	-24.4	0.05	0	Mecca Hills
7	74	-24.4	87	-24.4	0.05	0	North Shore
8	87	-24.4	90.5	-24.9	0.045	0	Durmid Hill 1
9	90.5	-24.9	94.0	-25.4	0.04	0	Durmid Hill 2
10	94	-25.4	97.5	-25.9	0.035	0	Durmid Hill 3
11	97.5	-25.9	101	-26.4	0.025	0	Durmid Hill 4
12	101	-26.4	104	-26.9	0.02	0	Durmid Hill 5
13	87	-24.4	104	-26.9	0.05	0	Durmid Hill
14	160	-8	200	-8	0.05	0	Imperial fault
15	104	-26.9	160	-8	0.025	0	Brawley seismic zone
16	101	-26.4	175	-38	0.025	0	San Andreas extension

Coordinate (43, 20.8) corresponds to 116°14.5' West and 33°47' North, and coordinate (102, -27.4) corresponds to 115°45' West and 33°23' North. Elements 5 to 13 describe the southern San Andreas fault. Figure 18*a* used elements 1-7 and elements 13 and 14. Figure 18*b* used the same elements excluding element 3. Figure 18*c* used the same elements as in Figure 18*b* but included elements 15 and 16. Figure 19*a* used the elements of Figure 18*a* but with reduced right-lateral slip (0.02) on segment 3. Figures 19*b* and 19*c* used elements 1-14 with reduced slip (0.02) on segment 3. In Figure 19*c* two cross faults were permitted to slip freely with an elliptical slip distribution.

motion on the southern San Andreas and Imperial "transform faults," resulted in the complete absence of any region of subsidence. Only models with strike-slip and no opening on the Brawley seismic zone are consistent with the location of the lowest part of the basin, and the amount of slip must be significantly less than the long-term slip on the Imperial and southern San Andreas faults. Numerically, the slip required on the Brawley seismic zone by our preferred models is 40% less than the long-term slip rate of the southern San Andreas at Indio. If we use a value of 25±10 mm/yr at Indio [*Sieh*, 1986] we find that the shear required on the Brawley seismic zone (10±2 mm/yr) is close the reported slip estimated from moment studies of seismic swarm activity on the fault in the last 40 years [*Johnson and Hill*, 1982].

The role of the observed cross faults in accommodating shear may be an important tectonic mechanism that has been overlooked in previous studies of this region. We show that two such faults, permitted to slip freely, are consistent with the location of the Salton trough. Because our models do not permit much slip on the San Andreas to extend south of Bombay beach, we suggest that cross faults must play an important role in the process that transfers San Andreas motion further south.

The results of models presented earlier assume that morphology can be related directly to the causal fault geometry. In our study of specific features of the San Andreas system in California we have found relations between fault geometries and associated morphology with scales from 5 to 50 km. Features exist at smaller and larger scales and could be modeled. However, caution must be exercised, particularly at larger scales. The effects of erosion, deposition, and

isostasy will be to modify the magnitude and, to some extent, the shape of large features. For example, the dominant source of sediment in the Salton Trough is from the south [*Sharp*, 1983], a process that is likely to bias northward the deepest part of the Salton Sea. We make no attempt to the estimate the effects of these surficial processes in interpreting our models. At large scales, isostatic compensation may suppress the magnitude of incipient hills and basins. Thus although we present models that reproduce the observed regions of uplift and subsidence effectively, the foregoing processes represent sources of error which we have not assessed.

CONCLUSIONS

Boundary element methods are used to derive a sequence of examples of dilatational strain fields associated with commonly occurring strike-slip fault zone features: bends, offsets, finite rupture lengths, and non uniform slip distributions. We use these basic "building blocks" to interpret the strain field associated with the general case of nonuniform slip within a fault zone of complex geometry. Ongoing dilatational strain is manifest as vertical motions of the Earth's surface near the fault zone. Basins are formed where dilatational strains result in an increase in surface area, and hills are created where dilatational strains result in a decrease in area.

We distinguish between the transient strains associated with fault rupture and the individually smaller but cumulatively significant strain fields that are associated with irregular fault zone geometry and contiguous long-term slip of the fault. These geometrically induced strain fields mould the topographic features of the fault zone for as long as their causative geometry persists. Coseismic strain fields are transient over the period of the earthquake cycle, and geometric strain fields persist for a time that is a function of the scale of the geometry and the slip rate on the fault. The two processes are separated in time by orders of magnitude.

In the absence of surficial processes the morphology of a fault zone is clearly the product of its geometry and slip distribution; where two are known the third may be inferred. However, we find that compressional features in nature are narrower than our models predict. The spatial scale along a feature is correct, but the scale normal to the feature is reduced. This decrease in aspect ratio is not observed in areas where we predict extensional dilatation. This may be due to errors in the assumption that linear behavior adequately approximates the deformation near to the fault, or we may have failed to include significant reverse faults in the modeling. Surficial processes and isostasy also introduce errors that we have not considered.

Nonetheless, major morphologic features in two areas on the San Andreas system are successfully modeled and lead to some inescapable conclusions about the slip distribution on mapped faults. In the Parkfield region we find we can emulate the topographic features of the fault zone best by permitting throughgoing slip reduced by 20% where it crosses the Cholame Valley. There is no significant long-term difference in the mean slip between Middle Mountain and the Cholame Valley and the contiguous San Andreas fault to the north and south. In the Coachella Valley we can emulate many of the features of the fault zone, but slip must be reduced on the southernmost San Andreas fault to explain the location of the Salton Sea. We require low slip on the Brawley seismic zone; similar to the slip rate inferred from estimates of microseismic moment release. Thus, according to our models, the Brawley seismic zone need not produce a major earthquake.

REFERENCES

Anderson, E. M., *The Dynamics of Faulting*, Oliver and Boyd, Edinburgh, 1951.

Babcock, E. A., Geology of the N.E. margin of the Salton Trough, Salton Sea, California, *Geol. Soc. Am. Bull.*, *85*, 321-332, 1974.

Bakun, W., and A. Lindh, The Parkfield, California, earthquake prediction experiment, *Science*, *229*, 619-624, 1985.

Bally, A.W., Seismic expression of structural styles, in *A.A.P.G. Sudies in Geology*, vol *15*, (3), American Association of Petroleum Geologists, Tulsa, Okla., 1983.

Bilham, R., and K. Hurst, Relationships between fault zone deformation and segment obliquity on the San Andreas fault, California, in *Proceedings of the China-United States Symposium on Crustal Deformation and Earthquakes*, edited by Wu Bing, pp. 510-524, Seismological Press, Beijing, 1988.

Bilham, R., and G. King, Slip distribution on oblique segments of the San Andreas fault, California: Observations and theory, *U. S. Geol. Surv. Open File Rep.*, in press, 1989.

Bilham, R., and P. Williams, Sawtooth segmentation and deformation processes on the southern San Andreas fault, California, *Geophys. Res. Lett.*, *12*, 557-560, 1985.

Bird, P., and R. W. Rosenstock, Kinematics of present crust and mantle flow in southern California, *Geol. Soc. Am. Bull.*, *85*, 321-332, 1984.

Brown, R.D., J. D. Vedder, R. E. Wallace, E. F. Roth, R. F. Yertes, R. O. Castle, A. O. Waananen, R. W. Page, and J. P. Eaton, The Parkfield-Cholame, California, earthquakes of June-August 1966 - Surface geologic effects, water resources aspects, and preliminary seismic data. *US. Geol. Surv. Prof. Pap.*, *579*, 1967.

Chinnery, M. A., The deformation of the ground around surface faults, *Bull. Seismol.Soc. Am.*, *51*, 355-372, 1961.

Clarke, M. M., Map showing recently active breaks of the San Andreas fault between Salton Sea and Whitewater River, Mission Creek, California, scale 1:24000, *US. Geol. Surv Misc. Invest. Ser. Map*, *I-1483*, 1984.

Crouch, S. L., and A. M. Starfield, *Boundary Element Methods in Solid Mechanics*, 332 pp. Allen and Unwin, Winchester, Mass., 1983.

Dibblee, T.W., Regional geology of San Andreas and related faults in Carrizo Plain, Temblor, Caliente, and La Panza Ranges and vicinity, California, *U. S. Geol. Surv. Misc. Geol. Invest. Map*, *I-757*, 1973.

Dickenson, W. R., Structural relationships of San Andreas fault system, Cholame Valley and Castle Mountain Range, California, *Geol. Soc. Am. Bull.*, *77*, 707-726, 1966.

Fuis, G. S., W. D. Mooney, J. H. Healy, G. A. McMechan, and W. J. Lutter, A seismic refraction survey of the Imperial Valley region, California, *J. Geophys. Res.*, *89*, 1165-1189, 1984.

Herzig, C. T., J. M. Mehegan, and C. E. Stelting, Lithostratigraphy of the State 2-14 borehole: Salton Sea Scientific Drilling Project, *J. Geophys. Res.*, *93*, 12,969-12,980, 1988.

Johnson, C. E. and D. P. Hill, Seismicity of the Imperial Valley, in The Imperial Valley Earthquake of Oct. 15,1979, *US. Geol. Surv. Professional Pap.*, *1254*, 15-24, 1982.

King, G.C.P., Speculations on the geometry of the initiation and termination processes of earthquake rupture and its relation to morphology and geological structure, *Pure Appl. Geophys.*, (3), *124*, 567-585, 1986.

King, G. C. P., R. S. Stein, and J. B. Rundle, The growth of geological structures by repeated earthquakes, 1, Conceptual framework, *J. Geophys. Res.*, *93*, 13,307-13,318, 1988.

Lachenbruch, A. H., J. H. Sass, and S. P. Galanis, Jr. Heat flow in southernmost California and the origin of the Salton Trough, *J. Geophys. Res.*, *90*, 6709-6736, 1985.

Lomnitz, C., F. Mooser, C. R. Allen, J. N. Brune, and W. Thatcher, Seismicity and tectonics of the northern Gulf of California region, Mexico *Geofis. Int.*, *10*, 37-48 1970.

Louie, J. N., R. Allen, D. C. Johnson, P. C. Haase and S. N. Cohn, Fault slip in southern California. *Bull. Seismol. Soc. Am.*, *75*, 811-832, 1975.

Mansinha, L., and D.E. Smylie, The displacement fields of inclined faults, *Bull. Seismol. Soc. Am.* *72*, 1433-1440, 1967.

Minster, J. B., and T. H. Jordan, Present-day plate motions, *J. Geophys. Res.*, *83*, 5331-5354, 1978.

Oppenheimer, D. H., P. A. Reasenberg and R. W. Simpson, Fault plane solutions for the 1984 Morgan Hill, California, earthquake sequence: Evidence for the state of stress on the Calaveras Fault, *J. Geophys. Res.*, *93*, 9007-9026, 1988.

Pollard, D. D., and P. Segall, Theoretical displacements and stresses near fractures in rock: with applications to faults joints, veins, dikes, and solution surfaces, in *Fracture Mechanics of Rock*, pp. 277-349, Academic, San Diego, Calif., 1987.

Rundle, J. B., Viscoelastic-gravitational deformation by a rectangular thrust fault in a layered Earth, *J. Geophys. Res.*, *87*, 7787-7796, 1982.

Rundle, J. B., A Physical Model for Earthquakes: 1. Fluctuations and Interactions, *J. Geophys. Res.*, *93*, 6237-6254, 1988.

Savage, J. C., Dislocations in seismology, in *Dislocations in Solids*, edited by F.R.N. Nabarro, pp. 253-339, North-Holland, Amsterdam, 1980.

Schulz, S. S., G. M. Mavko, R. O. Burford and W. D. Stuart, Long-term fault creep observations in central California, *J. Geophys. Res.*, *87*, 6977-6982, 1982.

Schwartz, D. P., and K. J. Coppersmith, Fault behavior and characteristic earthquakes: Examples from the Wasatch and San Andreas fault zones, *J. Geophys. Res.*, *89*, 5681-5698, 1984.

Sharp, R.V., Salton Trough tectonics and quaternary faulting, *US. Geol Surv. Open File Rep.*, *83-918*, 133, 1983.

Sieh, K. E., A review of geological evidence for recurrence times of large earthquakes, in *Earthquake Prediction: An International Review, Geophys. Monogr. Ser.*, vol 4, edited by D. Simpson and P. Richards, pp.181-207, AGU, Washington, D.C., 1981

Sieh, K. E., Slip along the San Andreas fault associated with the earthquake, in The Imperial Valley Earthquake of Oct. 15 1979, *US. Geol. Surv. Prof. Pap., 1254,* 155-160, 1982.

Sieh, K., Slip rate across the San Andreas fault and prehistoric earthquakes at Indio, California, *Eos Trans. AGU, 67,* 1200, 1986.

Stuart, W. D., Forecast model for large and great earthquakes in southern California, *J. Geophys. Res.*, *91,* 13, 771-13,786, 1986.

Sykes, L. R., and S. P. Nishenko, Probabilities of occurrence of large plate rupturing earthquakes for the San Andreas, San Jacinto, and Imperial faults, California 1983-2003, *J. Geophys. Res.*, *89,* 5905-5927, 1984.

Sylvester, A. G., Strike-slip faults, *Geol. Soc. Am. Bull., 100,* 1666-1703, 1988.

Sylvester, A. G., and R. R. Smith, Tectonic transpression and basement-controlled deformation in the San Andreas fault zone, Salton Trough, California, *Am. Assoc. Pet. Geol. Bull., 60,* 2081-2102, 1976.

Thatcher, W, and M. Lisowski, Long-term seismic potential of the San Andreas fault southeast of San Francisco, California, *J. Geophys. Res., 92,* 4771-4784, 1987.

Williams, P. L., S. McGill, K. Sieh, C. R. Allen, and J. L. Louie, Triggered-slip on the southern San Andreas after the 8 July 1986, North Palm Springs earthquake, *Bull. Seismol. Soc Am., 78,* 1112-1122, 1989.

R. Bilham, CIRES and Department of Geological Sciences, University of Colorado, Boulder, CO 80309.

G. King, U. S. Geological Survey, Box 25046, MS 966, DFC, Denver, CO 80225.